PROCEEDINGS, 51st Workshop on Geothermal Reservoir Engineering
Stanford University, Stanford, California, February 9-11, 2026
SGP-TR-230

Fracture Geometry Characterization in EGS: An Integrated Study Using Multiple Diagnostic Methods

Mingliang Han[1, *], Dana Jurick[2], Yuanyuan Ma[3], Artur Guzik[2], Jonathan Ajo-Franklin[3], Ge Jin[4], Kan Wu[1]

[1] Harold Vance Department of Petroleum Engineering, Texas A&M University, College Station, TX, USA

[2] Neubrex Energy Services, LLC., Bellville, TX, USA

[3] Department of Environmental and Planetary Sciences, Rice University, Houston, TX, USA

[4] Department of Geophysics, Colorado School of Mines, Golden, CO, USA

*liang25.am2024@tamu.edu

Keywords: Cross-Well Fiber-Optic Strain Monitoring; Enhanced Geothermal Systems (EGS); Hydraulic Fracture Geometry; Fracture–Natural Fracture Interaction

ABSTRACT

Multi-stage hydraulic fracturing is widely used in Enhanced Geothermal Systems (EGS) to create extensive fracture networks, which serve as flow pathways between injector and producer wells. Optimizing well placement requires reliable constraints on fracture geometry, such as height, length, and connectivity, which in EGS remains poorly understood due to limited direct observations. Cross-well distributed fiber-optic strain measurements in offset monitoring wells have proven highly effective for inferring fracture geometry and have reshaped understanding in unconventional reservoirs. In this study, we interpret cross-well fiber data acquired at the FORGE (Frontier Observatory for Research in Geothermal Energy) EGS site and integrate the results with microseismic locations and imaging results to characterize the stimulated fracture geometry.

We analyzed cross-well fiber strain data to identify fracture hits in the offset monitoring well. Fracture hits were detected using a multi-attribute approach combining strain rate, strain gradient, and displacement signals. An in-house forward geomechanics model has been used to simulate strain responses under varying conditions. This enables us to interpret the abnormal strain signatures observed in EGS that differ from the typical responses in unconventional reservoirs. We refined our interpretations with microseismic analysis and natural fracture characterization.

We have detected 21 fracture hits, which clustered within three depth intervals in the monitoring well—8,771–8,996 ft, 9,432–9,502 ft, and 9,742–9,787 ft—with inferred fracture spacing of ~15–35 ft. Many fractures reopened two to three times during late-stage pumping. On average, newly formed fractures reached the monitoring well after 132 minutes, whereas reopening occurred within 64 minutes. We generated a cross-section view by connecting perforation and fracture-hit location and calculated fracture dip angle, assuming the strike direction coincides with the maximum horizontal stress orientation of 78° relative to the wellbore toe side. The dip angles range from 58° - 102°, with only two fractures dipping toward the toe side. Forward geomechanical modeling using a fracture strike of 78° and dip of 60° reproduces the prominent asymmetric, heart-shaped strain signature observed in Stage 8. The consistency between the local and global dip angles indicates that the hydraulic fracture likely dips 59° from horizontal in stage 8, which is consistent with the conclusion drawn from the in-situ stress analysis. In the cross-sectional view, the inferred fracture propagation direction aligns well with the microseismic event distribution in Stages 3 through 7. However, in Stage 8, the fracture hits occurred first, followed by microseismic activity along a different trajectory. This observation indicates that the hydraulic fracture intersected the 16B well and reactivated a pre-existing natural fracture. The integrated analysis of Stages 8-10 supports the hypothesis that the local S_v is not the principal stress, which explains the hydraulic fracture dipping 59° observed in Stage 8.

Our results advance understanding of fracture propagation and geometry in EGS and highlight the value of distributed fiber-optic sensing (DFOS) for geothermal fracture diagnostics. The findings provide key inputs for optimizing injector–producer placement, including both vertical and horizontal well spacing.

1. INTRODUCTION

Enhanced Geothermal Systems (EGS) rely on hydraulic stimulation to create, reopen, and interconnect fracture networks in low-permeability hot rock, thereby establishing effective hydraulic pathways between injection and production wells and enabling sustainable heat extraction. The geometry and hydraulic properties of these fractures—including fracture length, height, spatial distribution, and conductivity—govern fluid circulation patterns, heat sweep efficiency, and long-term reservoir performance. A robust understanding of fracture geometry is therefore fundamental to evaluating stimulation effectiveness and predicting reservoir behavior in EGS. In particular, fracture dimensions and connectivity directly control the effective stimulated reservoir volume and the degree of thermal and hydraulic interaction between wells. These factors, in turn, determine optimal horizontal and vertical well spacing and ultimately affect both energy recovery and economic viability.

A range of methods has been applied to evaluate hydraulic stimulation outcomes and characterize fracture geometry in EGS and unconventional reservoirs. In-situ stress analysis, derived from wellbore observations and geophysical measurements, provides first-order constraints on fracture orientation and propagation tendency (Zoback, 2010; Xing et al., 2022). Forward geomechanics modeling has been widely used to simulate fracture initiation and growth under prescribed stress states and rock properties (Rutqvist et al., 2013; Zhang et al., 2022). The spatial and temporal distribution of microseismic events provides indirect constraints on where and how fractures propagate in three-dimensional space (Maxwell, 2014; Bao and Eaton, 2016). In recent years, cross-well distributed fiber-optic strain measurements acquired in offset monitoring wells have emerged as a powerful tool with high temporal and spatial resolution for inferring hydraulic fracture geometry. Deployment along the wellbore enables direct measurement of strain responses associated with fracture propagation (Karrenbach et al., 2017; Jin and Roy, 2017). Because fiber-optic measurements record in-situ subsurface strain, they offer a more accurate and reliable constraint on induced fracture geometry than surface-based or seismic observations. Applications in unconventional reservoirs have demonstrated that fiber-based measurements can significantly refine interpretations of fracture extent, complexity, and stage-to-stage variability (Wu et al., 2021; Ning et al., 2024).

The Utah FORGE site serves as a scientific testbed for EGS, providing a unique opportunity to investigate fracture geometry and stimulation mechanisms in geothermal reservoirs. To systematically promote fracture development and enhance reservoir connectivity, multi-stage hydraulic stimulation has been implemented at the site. The project has produced exceptionally comprehensive fracture diagnostic datasets, collected by multiple institutions and investigated by numerous research groups, to advance the understanding of fracture geometry and evolution. Distributed fiber-optic sensing data acquired from two fiber cables have been used to investigate reservoir connectivity (Xing et al., 2025; Ou et al., 2024) and hydraulic propagation (Ghassemi et al., 2025; Jurick et al., 2025). Two independent microseismic event catalogs have been employed to constrain the spatial distribution of hydraulic and natural fractures (Ajo-Franklin et al., 2025; McClure et al., 2025). In addition, borehole image logs, including Formation Micro-Imager (FMI) and Ultrasonic Borehole Imager (UBI) data, have been used to characterize the in-situ stress state and fracture orientations (Xing et al., 2022). Despite these advances, a fully integrated interpretation that synthesizes fiber-optic observations, stress constraints, numerical modeling, and microseismicity into a unified and physically consistent description of fracture propagation has not yet been achieved. This gap highlights the need for a holistic framework to reconcile multi-physics datasets and improve our understanding of fracture evolution in EGS reservoirs.

In this study, we developed an integrated workflow that combines multiple diagnostic methods to interpret hydraulic fracture propagation during multi-stage stimulation at the FORGE site. By leveraging the complementary strengths of these datasets, this work aims to reduce interpretational ambiguity and provide a more robust characterization of fracture propagation and hydraulic fracture–natural fracture interaction in EGS reservoirs.

The fracture geometry characterization workflow consists of the following steps in Figure 1. Step 1: Fracture-hit number, locations, and timing are identified through cross-well fiber-optic data analysis. Fracture dip angles are then calculated by directly connecting the perforation and fracture-hit locations. Step 2: A sensitivity analysis is performed to investigate the effect of fracture dip angle on the strain-response pattern. The dip angle that is closest to the value calculated in Step 1 successfully reproduces the strain pattern observed in the field data. Step 3: Microseismic events are integrated with the identified fracture hits and their spatial distribution and temporal evolution are analyzed to validate the inferred fracture locations and the connectivity between hydraulic fractures and natural fractures/faults.

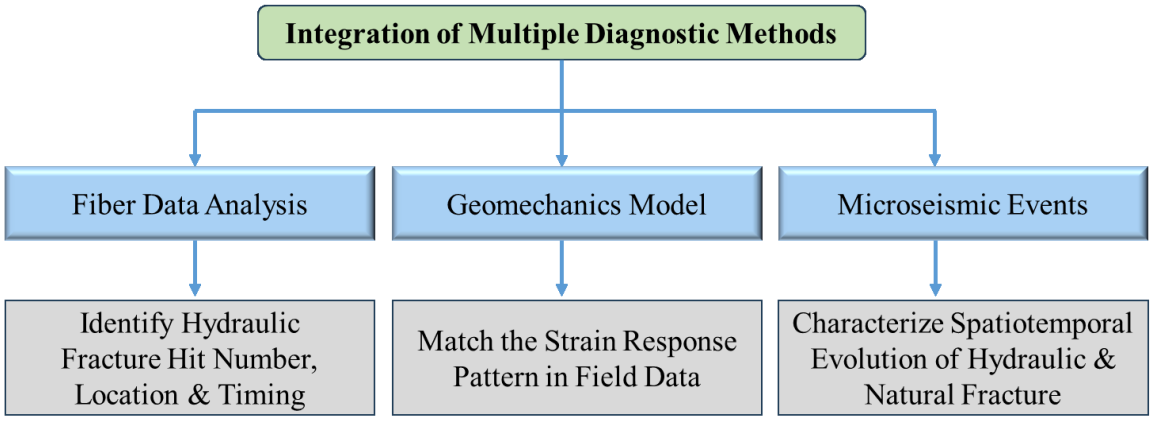

Figure 1: Integrated workflow for fracture geometry characterization using multiple diagnostic methods.

2. FIELD DESCRIPTION

At Utah FORGE site, well 16A served as the injection well and was hydraulically stimulated. Well 16B serves as the monitoring/production well and is equipped with two fiber-optic cables to record strain responses associated with induced fracture propagation. Wells 16A and 16B are nearly parallel, which can be clearly observed from both the side view and the 3D view shown in

Figure 2. Perforation locations are marked along the trajectory of well 16A as colored points. It is important to note that both wells are deviated rather than horizontal, with an inclination of approximately 26° from the horizontal, as shown in Figure 2. In the inclined section, the horizontal and vertical offsets between the two wells are approximately 30 ft and 350 ft, respectively.

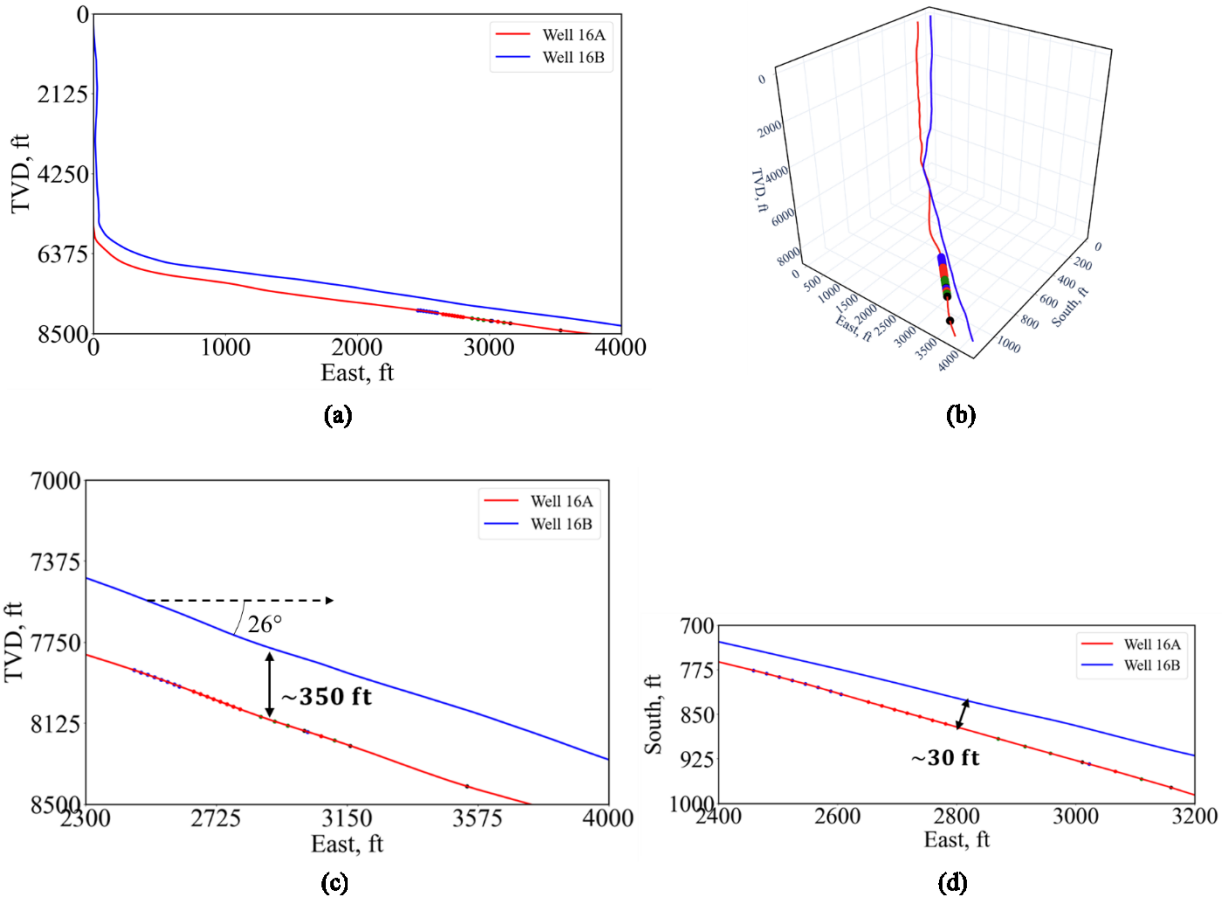

Figure 2. Well trajectories of Wells 16A and 16B at the Utah FORGE site: (a) side view, (b) 3D view, (c) zoomed-in side view, and (d) zoomed-in map view. Colored markers along Well 16A indicate perforation locations for the eight stimulation stages.

The map-view azimuth of the well trajectory is approximately S77°E. According to previous studies (Podgorney et al., 2020; Xing et al., 2022), the maximum horizontal stress is oriented at approximately N25°E. Assuming that the hydraulic fracture strike aligns with the direction of the maximum horizontal stress (S_{Hmax}), the expected fracture orientation is illustrated in Figure 3. The angle between the fracture strike and Well 16B is approximately 78°, indicating a well–fracture configuration that is close to, but not exactly, perpendicular.

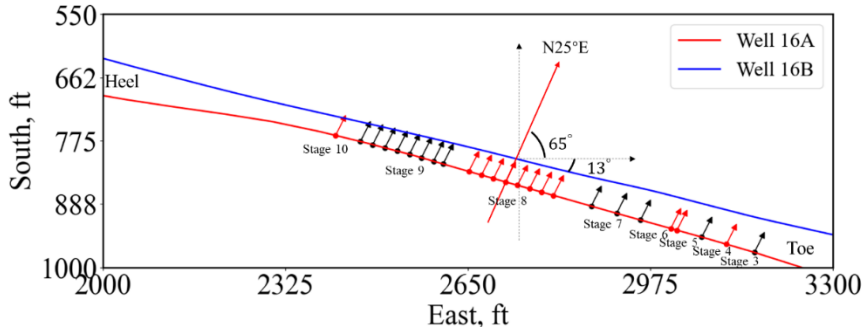

Figure 3. Map view of hydraulic fracture orientation, assuming that the fracture strike is aligned with the maximum horizontal stress (S_{Hmax}).

8 stages were stimulated along 16A well during April 2024. What should pay attention is that stage 3 was re-stimulated, and the first cluster is far away from the other, so only the second cluster in stage 3 is considered in later study. The cluster number and cluster spacing

in each stage are summarized in Table 1. The pumping curve, including wellhead treatment pressure, proppant concentration, and slurry rate are shown in Figure 4.

Table 1: Summary of completion design in Forge project in April 2024.

Stage	Cluster Number	Cluster Spacing/ft
3R	2	440
4	1	/
5	1	/
6	2	13
7	3	50
8	8	25
9	8	24
10	1	/

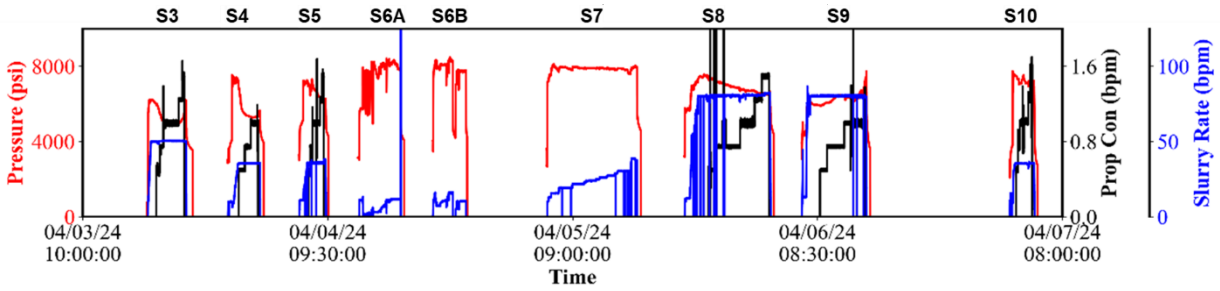

Figure 4. Pumping curves for the 8 stimulation stages at the Utah FORGE site, showing wellhead treatment pressure, proppant concentration, and slurry rate during multi-stage hydraulic stimulation.

3. ANALYSIS OF CROSS-WELL DISTRIBUTED FIBER-OPTIC STRAIN MEASUREMENT

3.1 Fracture Hit Identification

The strain-rate data measured by Rayleigh Frequency Shift Distributed Strain Sensing (RFS-DSS) are presented in Figure 5(a), focusing on the depth interval from 8,000 ft to 10,000 ft, where the most pronounced deformation responses are observed. This depth range corresponds to the primary zone of fracture activity and associated rock deformation during stimulation. The permanent fiber-optic cable deployed in Well 16B is characterized by a gauge length of 0.66 ft, a spatial sampling interval of 0.33 ft, and a temporal resolution of 30 s. These acquisition parameters provide exceptionally high spatiotemporal resolution, enabling detailed tracking of strain evolution along the wellbore. The black dashed boxes indicate the expected fracture-hit corridor, if the induced fractures propagate vertically and align with the S_{Hmax} direction, as discussed above, which represents the typical expectation. However, most of the responses are out of these boxes, indicating the fracture propagation is more complex than expected. The corridors in stage 3-6 almost occur at the same measured depth, meaning the fractures initially generated at stage 3 are reopened in later stages. The pumping curve in Figure 5(b) is used to identify the beginning and shut-in moment in each stage of the waterfall.

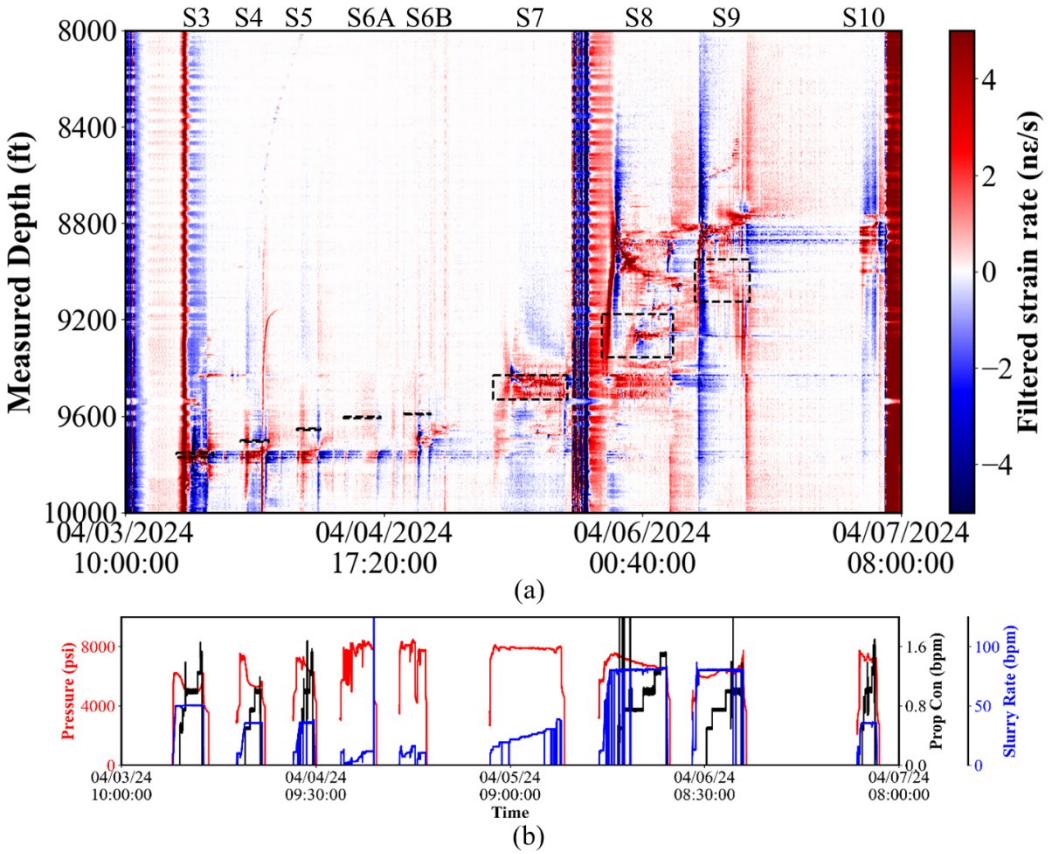

Figure 5. (a) Strain-rate waterfall from the permanent fiber. The black dashed boxes indicate the expected fracture-hit corridor. (b) Pumping curves across all stimulation stages.

Fracture-hit detection is a key application of fiber-optic data and provides a direct and reliable constraint on fracture geometry. Strain responses associated with fracture propagation vary both spatially and temporally, and they differ significantly between newly created fractures and the reopening of pre-existing fractures. Figure 6(a) shows the strain-rate response induced by a newly propagating fracture approaching from a distance, intersecting the fiber perpendicularly, and eventually closing. This process produces a distinct, symmetric heart-shaped pattern of extension prior to fracture hit, followed by a narrow band of extension surrounded by compression as the fracture arrives and continues to propagate. This pattern subsequently reverses during fracture closure. In contrast, Figure 6(b) illustrates the strain-rate response associated with the reopening and subsequent closure of a pre-existing fracture that also intersects the fiber perpendicularly. In Figure 6(b), a pointed extension pattern, instead of a heart-shaped pattern, is observed at the fracture location, suggesting fracture reopening (Haffener et al., 2022).

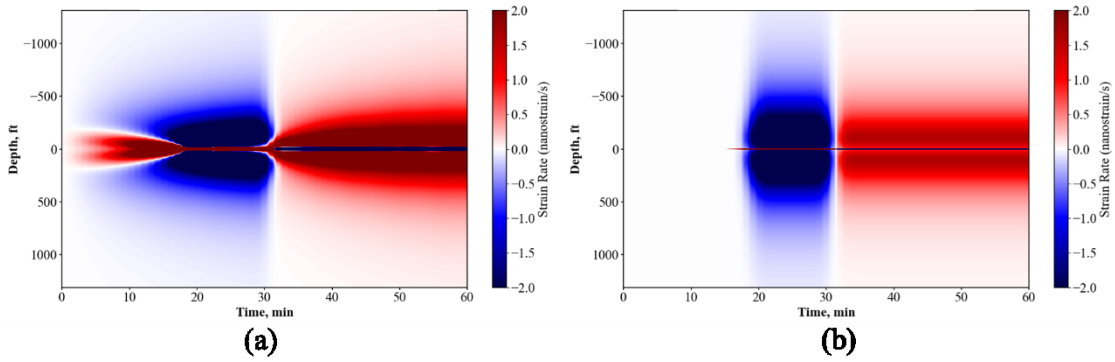

Figure 6: Strain rate waterfall from forward geomechanics simulation (a) new fracture hit and closure (b) pre-existing fracture reopening and closure.

Based on the strain-response information, multiple methods were employed to identify fracture-hit locations and timings. In this study, Song's method is adopted, in which strain rate, integrated positive strain, strain gradient, pumping curves, and maximum strain gradient are quantitatively analyzed (Song et al., 2025). Stage 10 is used as an example, as shown in Figure 7. The extensional zone observed during pumping is composed of multiple discrete linear features. No typical heart-shaped pattern is observed in the filtered strain-rate waterfall for Stage 10, indicating that the recorded responses are associated with the reopening of pre-existing fractures rather than the generation of new ones. This interpretation is further supported by strain-rate responses observed at the same locations during earlier stages (e.g., Stage 9), confirming that these fractures were previously generated. The identified fracture-hit locations are marked by black dashed lines in Figure 7(a).

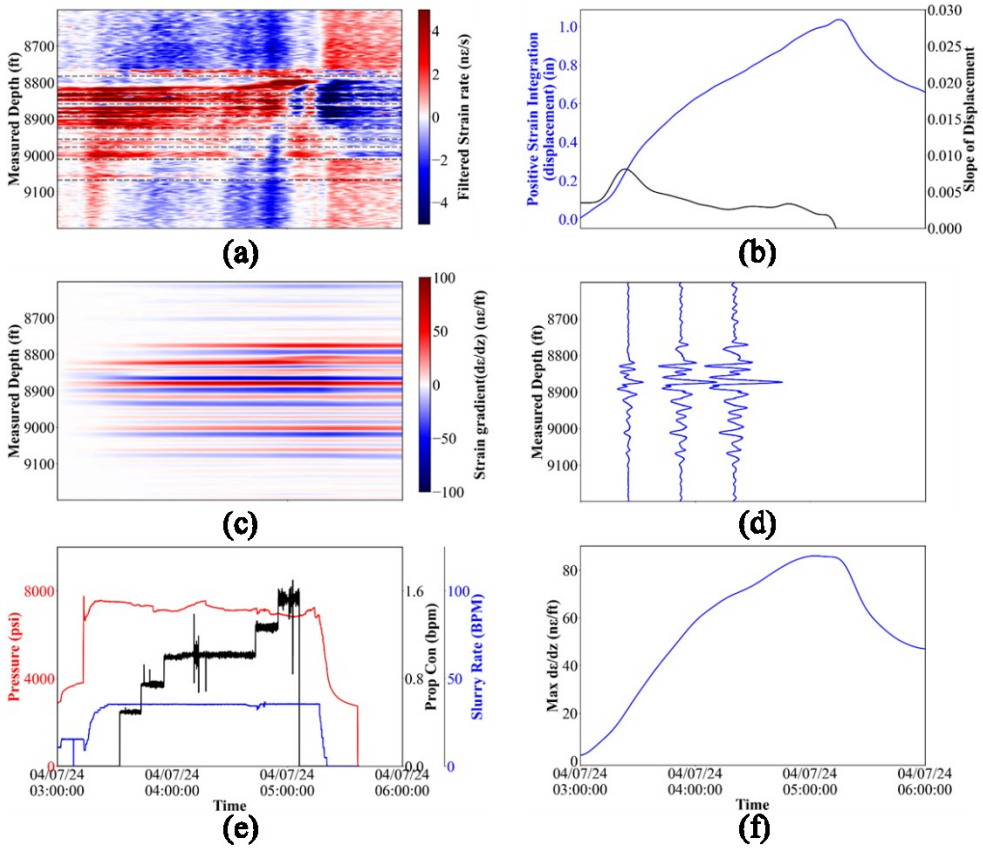

Figure 7. Fracture-hit detection in Stage 10 using multiple parameters: (a) strain rate, (b) positive strain integration, (c) strain gradient, (d) strain gradient at three selected time points, (e) pumping curves, and (f) maximum strain gradient (Song et al., 2025).

Applying this method to all stages, a total of 21 fracture-hit events were identified, all of which are marked with black dashed lines in the waterfall as shown in Figure 8. Most of the identified fracture-hit locations are consistent with those reported in previous studies using different identification methods (Jurick et al., 2025). The fracture hits are clustered into three groups: 8,771–8,996 ft (average fracture-hit spacing of 31 ft), 9,432–9,502 ft (average spacing of 34 ft), and 9,742–9,787 ft (average spacing of 15 ft). The number of perforation clusters, new fracture hits and pre-existing fracture reopening are summarized in Figure 9. The number of perforation clusters is lower than the number of induced fractures in Stage 3, equal in Stages 6–8, and higher in the remaining stages. No new fracture hits are generated in Stages 4, 5, and 10. The average time for new fractures to reach the monitoring well (16B) is 132 minutes, while the average time for pre-existing fracture reopening at 16B is 64 minutes.

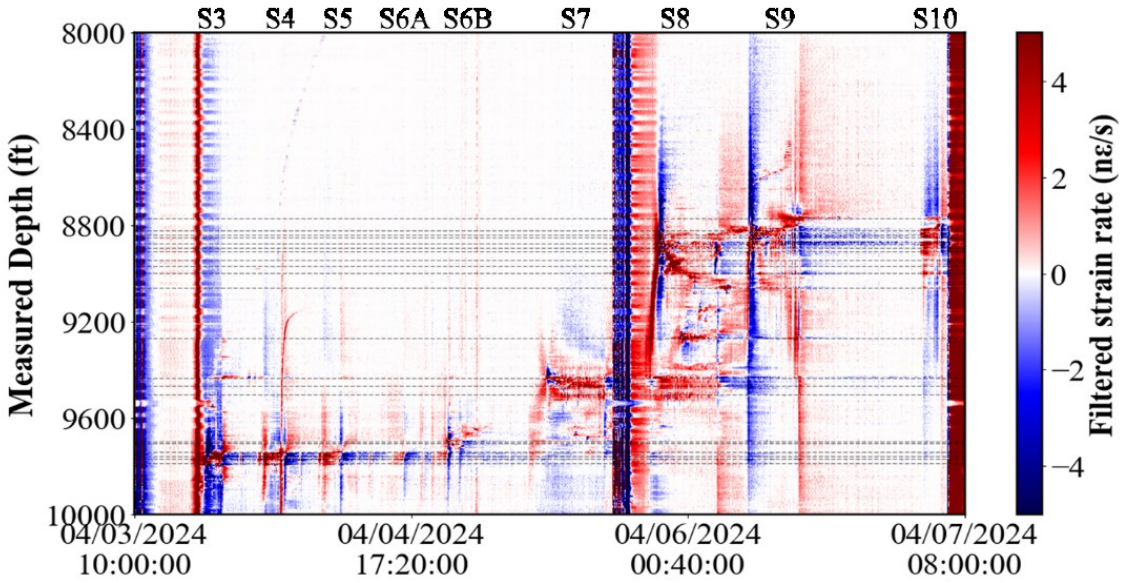

Figure 8: Strain-rate waterfall from the permanent fiber at well 16B. The black dashed lines indicate the identified fracture hits.

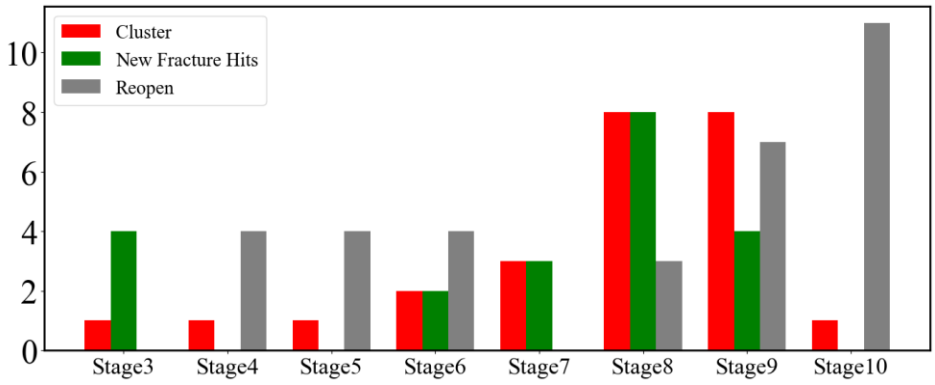

Figure 9: Number of fracture clusters, new hits, and reopened fractures in each stage.

3.2 Fracture Dip Angle Determination

Although the perforation and fracture-hit locations have been determined, the propagation path of the fracture between these points remains uncertain. When the fracture hit is located nearly directly above the perforation as shown in Figure 10(a), such as stage 3 in field data, we can assume the fracture directly propagated towards the hit location. When the fracture hit is located obliquely above the perforation, as observed in Stage 8 field data, three hypotheses for the potential propagation paths are proposed, as shown in Figure 10(b).

Path (a): Assuming the presence of cement debonding along the treatment wellbore, the fracturing fluid initially migrates upward along the wellbore and then propagates outward, approximately perpendicular to the wellbore, to reach the fracture-hit location.

Path (b): Assuming that the local vertical stress is not the principal stress, the fracturing fluid propagates directly toward the fracture-hit location along an inclined fracture plane, with a dip angle deviating from 90°.

Path (c): Assuming cement debonding along the monitor wellbore, the fracturing fluid first propagates outward from the treatment wellbore and reaches the monitor well. It then migrates along the monitor wellbore to the fracture-hit location, inducing the observed strain response on the fiber.

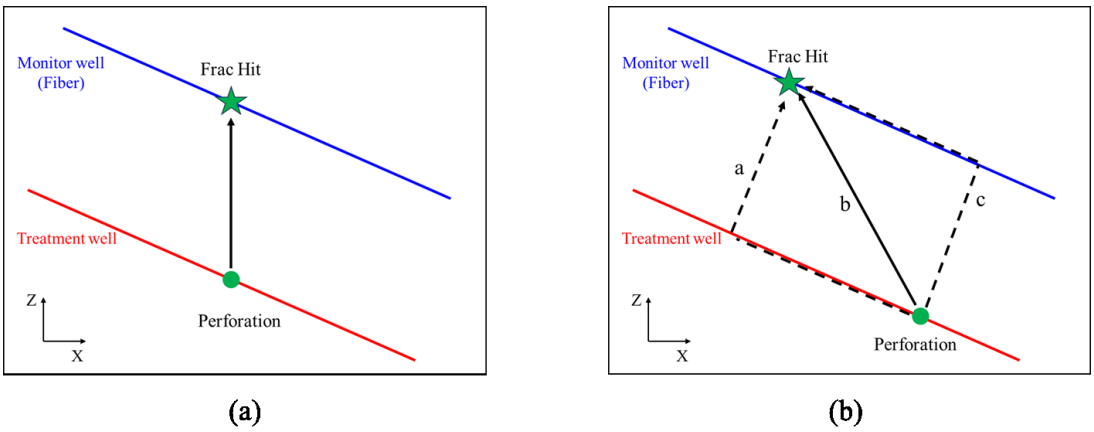

Figure 10: Side view of potential fracture propagation paths: (a) fracture hit located nearly directly above the perforation (b) fracture hit located obliquely above the perforation.

Path (b) in Figure 10(b) is adopted and validated in this study. The remaining paths shown in Figure 10(b) are discussed and ruled out as unreasonable in Section 6. Figure 11 shows the fracture planes (fracturing fluid flow paths) by connecting perforation and fracture hit locations. For example, 4 fracture hits initially generated in stage 3 but they reopened through stage 4-6. For new fracture hits, perforations and fracture-hit locations were paired on a one-to-one basis within each stage, although the numbers are not always equal. For reopening of pre-existing fractures, the starting point was assumed to be the midpoint of the stage, because it is difficult to determine which specific perforation reactivated a given pre-existing fracture.

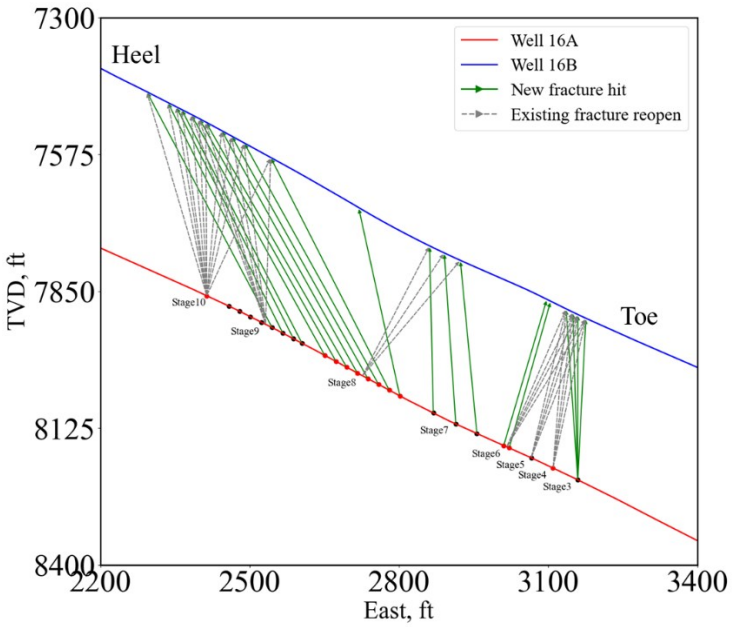

Figure 11: Side view of inferred hydraulic fracture propagation by connecting perforation and fracture hit locations. Green arrows indicate newly generated fracture hits, while gray dashed arrows indicate reactivated pre-existing fractures. Well trajectories of Well 16A and Well 16B are shown by red and blue lines, respectively, and perforation locations for all stages are marked by colored points.

By combining the perforation locations, identified fracture-hit locations, and strike angles, the fracture dip angles (measured from the horizontal plane to the fracture plane) were calculated and are shown in Figure 12. The dip angles range from 58° to 102°, where values greater than 90° indicate fractures tilted toward the toe. An observation is that the hydraulic fractures generated in stage 3-7 are vertical or subvertical, while those in stage 8-10 have a dip angle of about 60°.

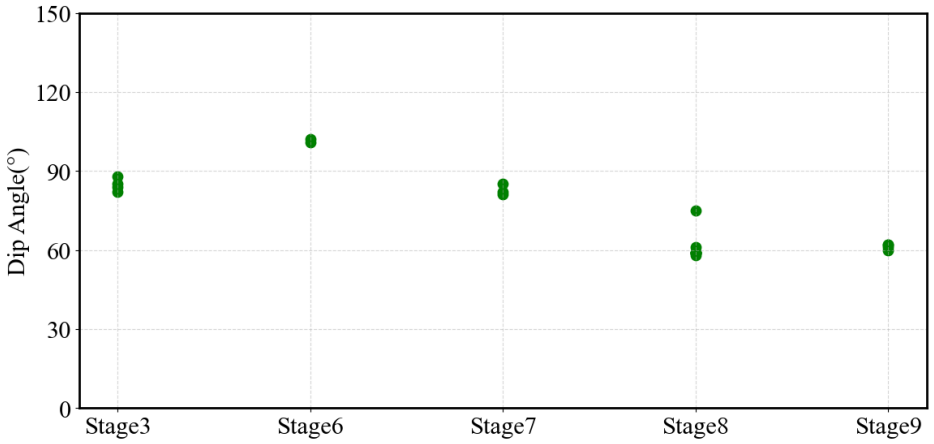

Figure 12: Summary of dip angles for all induced fractures. Stages not shown indicate that no new hydraulic fractures were generated.

4. FORWARD GEOMECHANICS MODELING

4.1 Model Setup and Parameterization

In this study, the forward geomechanics simulation is performed with an in-house simulator (Liu et al., 2021), which is developed based on the Three-Dimensional Displacement Discontinuity Method (3D DDM). 3D DDM is a boundary-element–based numerical approach widely used for modeling fracture propagation in elastic media. In 3D DDM, fractures are represented as displacement discontinuities embedded within a continuous elastic medium, enabling fracture opening and slipping to be directly related to the induced stress and displacement fields. By discretizing only the fracture surfaces rather than the entire domain, 3D DDM achieves high computational efficiency while accurately capturing induced stresses, strains, and displacements associated with fracture geometry. This makes DDM particularly well-suited for forward geomechanics simulations of strain evolution and strain-rate responses along fiber-optic sensing paths.

Figure 13 shows the strain-rate waterfall and pumping curve for Stage 8. The strain-rate pattern in this stage is of particular interest because it exhibits a distinct asymmetric heart-shaped feature and occurs at a location offset from the expected position, as shown in Figure 5(a). Consequently, a series of forward simulations were performed to reproduce this pattern, using Stage 8 as a representative example to validate the inferred fracture geometry.

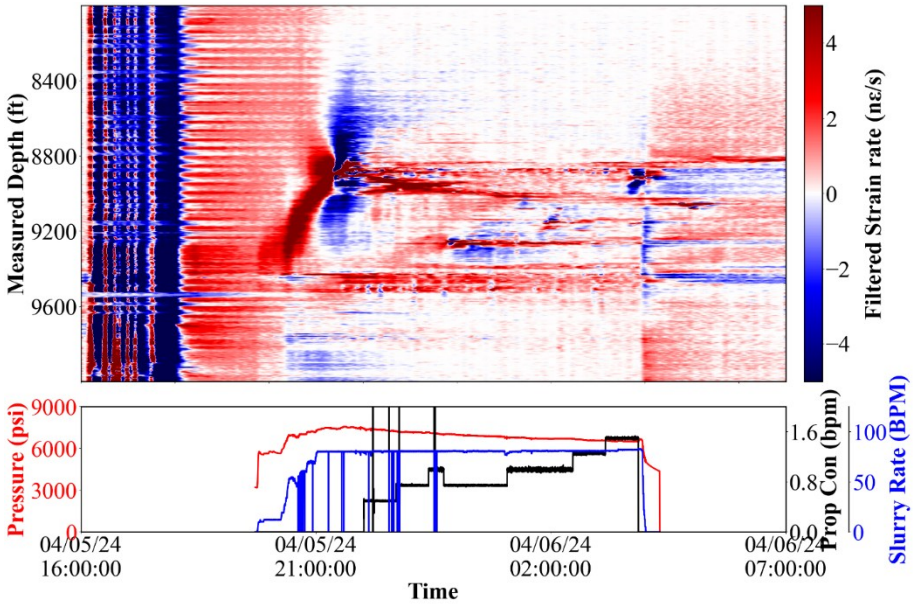

Figure 13: Zoomed-in view of the strain-rate waterfall and pumping curves for Stage 8

The hydraulic fractures are modeled with an elliptical geometry that expands uniformly over time in length, height, and width. The strike and dip angles are explicitly controlled to investigate the effect of fracture orientation on the induced strain-response pattern. The 3D view of fracture propagation is shown in Figure 14, and the corresponding fracture geometries are summarized in Table 2. The fracture

approaching angle is defined as the angle between the fracture plane and the wellbore, accounting for the wellbore dip angle of 26°, as shown in Figure 2(c). The fracture strike is assumed to align with the direction of the maximum horizontal stress (S_{Hmax}). A range of dip angles was tested to reproduce the asymmetric heart-shaped strain response observed in Stage 8.

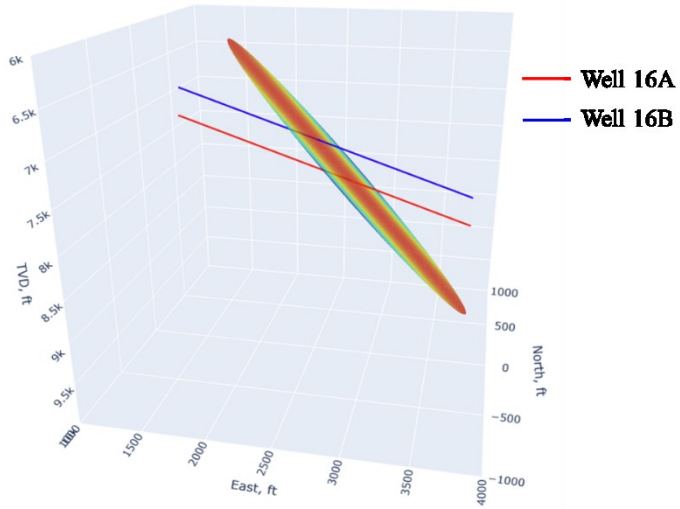

Figure 14: 3D view of the well location and fracture propagation. Color on the fracture plane indicates fracture width.

Table 2: Input of fracture geometry in simulation.

Half Length/ft	100
Upper Height/ft	800
Width/inch	0.1
Strike Angle/°	78°
Dip Angle/°	45°, 50°, 55°, 60°, 75°, 90°
Fracture Approaching Angle/°	19°, 24°, 29°, 34°, 49°, 64°

4.2 Simulation of Asymmetric Heart Shape

All strain-rate waterfalls shown in Figure 15 exhibit an asymmetric heart-shaped pattern, which differs from that in Figure 6(a) because the fracture simulated in Figure 15 is not perpendicular to the wellbore in either strike or dip. Start from Figure 15(a) with a fracture dip angle of 90°, the strain rate pattern is close to symmetric heart shape. With the dip angle decreasing, the heart shape gradually tends to be asymmetric with a shift angle. In particular, additional compressional responses appear in the central indentation of the heart-shaped pattern in Figures 15(e) and 15(f).

Among all the cases in Figure 15, the pattern obtained with a dip angle of 60° most closely matches the field observations in terms of both the size and the shift angle of the heart shape. This simulated dip angle is nearly identical to the dip angle inferred from connecting the perforation locations and fracture-hit locations, as discussed in Section 3.2. It should be noted that the dip angle in the simulation represents the local interaction angle between the fracture plane and the wellbore at the moment the fracture reaches the monitoring well, whereas the dip angle derived from field data is a global dip angle inferred from the perforation and fracture-hit locations. The consistency between the local and global dip angles supports the assumption that the fractures are inclined at approximately 59° and propagate directly toward Well 16B. In the simulations shown in Figure 15, fractures are modeled as purely tensile openings. Additional simulations incorporating combined tensile opening with strike-slip shearing and with dip-slip shearing were also conducted. However, shear components were found to be unnecessary for reproducing the strain-rate patterns observed in the field.

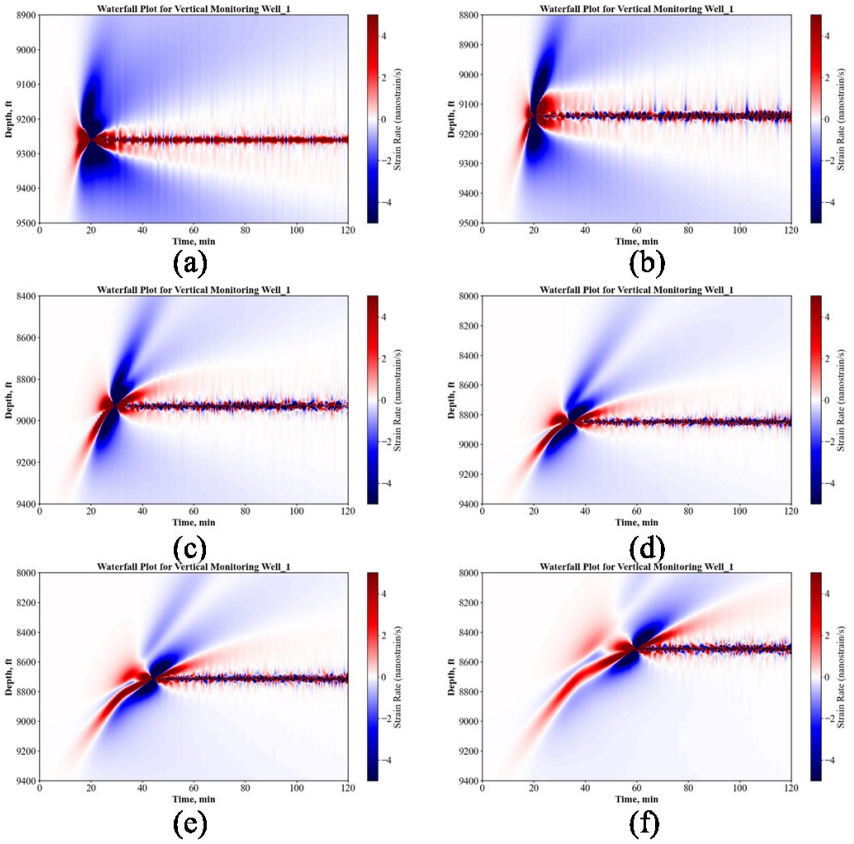

Figure 15: Simulated strain rate waterfall with different dip angles of hydraulic fractures (a) 90° (b) 75° (c) 60° (d) 55° (e) 50° (f) 45°.

5. INTEGRATED INTERPRETATION WITH MICROSEISMICITY

Microseismic data have been acquired and interpreted by several research groups. The overall interpretations of microseismic event distributions and the main conclusions are largely consistent across studies. The primary difference lies in the number of detected events. In this study, we use one microseismic catalog to validate fracture propagation and to investigate the interaction between hydraulic fractures and natural fractures, whose presence at the site has been demonstrated in previous studies (Ma et al., 2025).

5.1 Microseismic Event Distribution During Stage 8

Figure 16 shows the microseismic events (red circles) and hydraulic fracture activities (red arrows) identified from fiber-optic data analysis, integrated with the well trajectories (red (well 16A) and blue lines (Well 16B)) and perforation locations (colored triangles). Figure 16(a) shows a side view of all events during Stage 8, which can be divided into three regions indicated by blue, green, and black dashed ellipses. Figure 16(b) presents a three-dimensional view at a moment when the inferred hydraulic fracture plane extends and intersects the pre-existing natural fracture or fault plane at the intersection zone.

In the blue ellipse of Figure 16(a), the microseismicity delineates a natural fracture zone, which has been widely agreed in previous studies. The green ellipse highlights the inferred hydraulic fracture planes in Stage 8. Only a limited number of microseismic events are observed in the upper half of the green ellipse, whereas a significantly higher density of events occurs in the lower half. This different distribution is interpreted to result from differences in fracture mechanisms. In the upper half, fracture propagation is dominated by tensile opening associated with newly generated hydraulic fractures, which is largely aseismic and therefore poorly represented in the microseismic dataset. In contrast, in the lower half, the newly generated hydraulic fractures are likely connected to fractures activated during earlier stages, leading to a combination of tensile opening and shear slip. The shear component produces abundant microseismic events, resulting in the observed higher event density. The black ellipse highlights the pathway of pre-existing fracture reopening. Although the data points are scattered, they suggest a potential trend. This tendency, indicated by the green and black ellipses, can be more clearly observed in Figure 18.

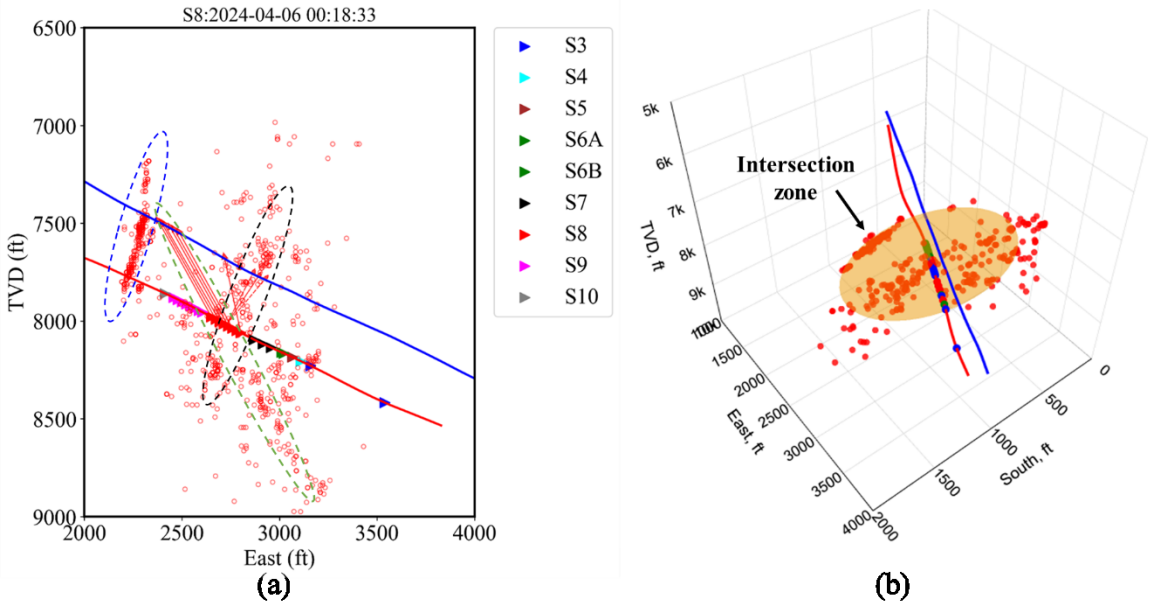

Figure 16: (a) Side view of microseismic event distribution (confidence index > 50) and inferred hydraulic fractures in Stage 8. (b) Three-dimensional view at a moment shortly after the hydraulic fracture intersects the natural fracture. Microseismic events during stage 8 are shown as red circles, and hydraulic fractures inferred from fiber-optic data are indicated by red arrows. Well trajectories of Well 16A and Well 16B are shown by red and blue lines, respectively, and perforation locations for all stages are marked by colored triangles. The orange plane in (b) indicates the inferred hydraulic fracture plane.

When we investigate the temporal evolution of fracture hits in Figure 17, it also supports the consistency and shows how the hydraulic fractures interact with the natural fracture. In Figure 17, panels (a) through (f) represent progressively increasing pumping times. The time intervals between panels are defined according to the fracture-hit times and vary from 8 minutes to 6 hours. In Figure 17(a), three pre-existing hydraulic fractures (red dashed arrows) are reopened, which induce some microseismic events near them. At this moment, some other microseismicity on the downward side is induced by the propagation of new hydraulic fractures, which have not hit the fiber and are not marked as arrows. As far, the natural fracture has not been activated.

In Figure 17(b), a solid red arrow marks the first hydraulic fracture hit on the fiber. At the same time, a limited number of microseismic events are observed within the natural fracture region between the treatment and the monitoring wells, suggesting that the hydraulic fracture plane intersected a pre-existing natural fracture plane. As a result, fracturing fluid likely entered and activated the natural fracture. The three-dimensional location is shown in Figure 16(b), where the intersection zone highlights the first region where the extending hydraulic fracture plane contacts the natural fracture plane.

Figure 17(c) shows the occurrence of the second new fracture hit, accompanied by further extension of the natural fracture. A higher density of microseismic events is observed. Figure 17(d) shows the occurrence of the third, fourth, and fifth new fracture hits, accompanied by continued extension of the natural fracture. An increased number of microseismic events is observed. Figure 17(e) shows the occurrence of the sixth new fracture hit with continued natural fracture extension, along with further clustering of microseismic events. Figure 17(f) shows the occurrence of the seventh and eighth new fracture hits with continued natural fracture extension. At this stage, the overall trend of microseismic event distribution becomes clearly defined.

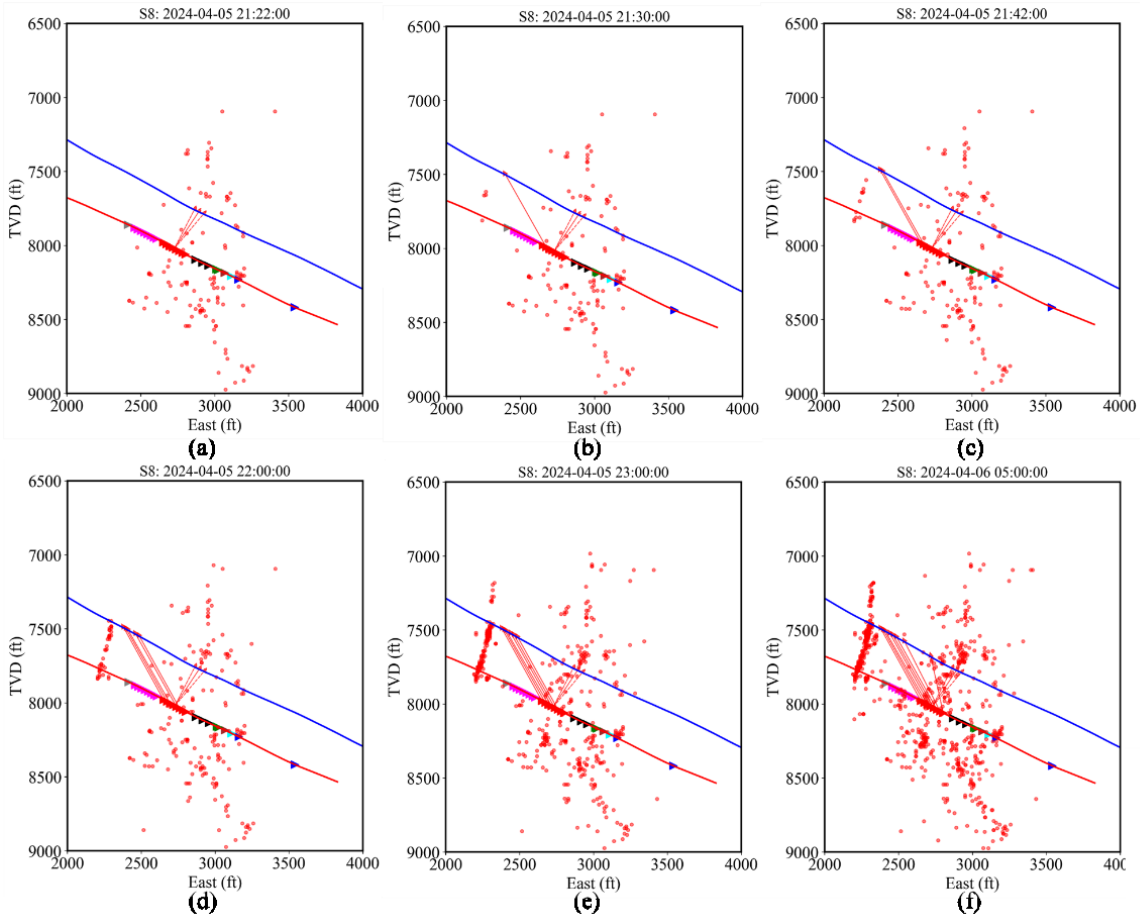

Figure 17: Spatiotemporal distribution of microseismic events and inferred hydraulic fracture planes (fluid flow path) during stage 8: (a) reopening of three pre-existing fractures; (b) occurrence of the first new fracture hit and activation of the natural fracture; (c) occurrence of the second new fracture hit accompanied by further extension of the natural fracture; (d) occurrence of the third, fourth, and fifth new fracture hits accompanied by further extension of the natural fracture; (e) occurrence of the sixth new fracture hit with continued natural fracture extension; (f) occurrence of the seventh and eighth new fracture hits with continued natural fracture extension. Note: The symbols are the same as those used in Figure 16.

5.2 Microseismic Events Distribution Across All Stages

Figure 18 integrates all inferred fracture planes with microseismic events across all stages, showing a generally consistent spatial distribution. In Stages 3–7, both newly induced fractures and reactivated pre-existing fractures are nearly vertical. In contrast, in Stages 8–10, hydraulic fractures are significantly tilted toward the heel. This change in fracture orientation suggests that the principal stress distribution is not uniform, likely influenced by natural fractures or faults. Fracture imaging using DAS microseismic sources (Ma et al., 2026) further confirms the existence of the inferred hydraulic and natural fracture/fault planes in Stages 8–10. Figure 19 shows the fracture imaging results with the fracture connection map overlaid. The blue line (Zone 3) represents some hydraulic fracture events during Stage 8, which aligns with the fracture reopening inferred from the RFS-DSS data as described in section 3.1 (Figure 17a). Farther west, a natural fracture or small fault (red line, Zone 1) is imaged at a nearby location consistent with both the fracture hit (Figure 17b) and the associated microseismic cloud (Figure 16a). The imaging results show relatively weak reflected energy along the fracture connection, which suggests the presence of a potential low-angle connector (Zone 2) linking the injection interval to the natural fracture.

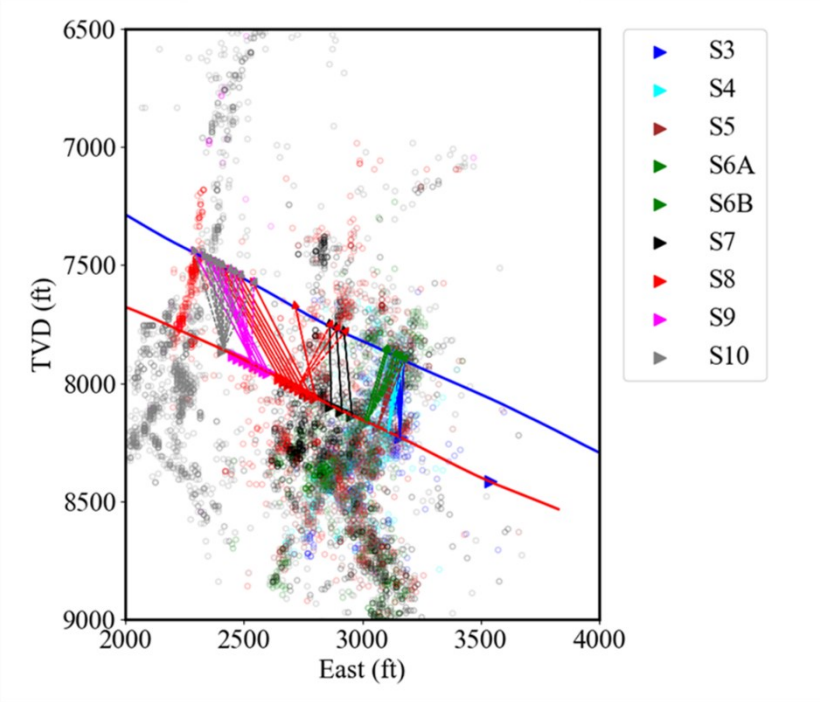

Figure 18: Side view of microseismic events distribution (colored open circles) and inferred hydraulic fracture propagation (colored arrows). Different colors correspond to different stimulation stages. Solid arrows indicate newly generated fractures, whereas dashed arrows represent reopening of pre-existing induced fractures.

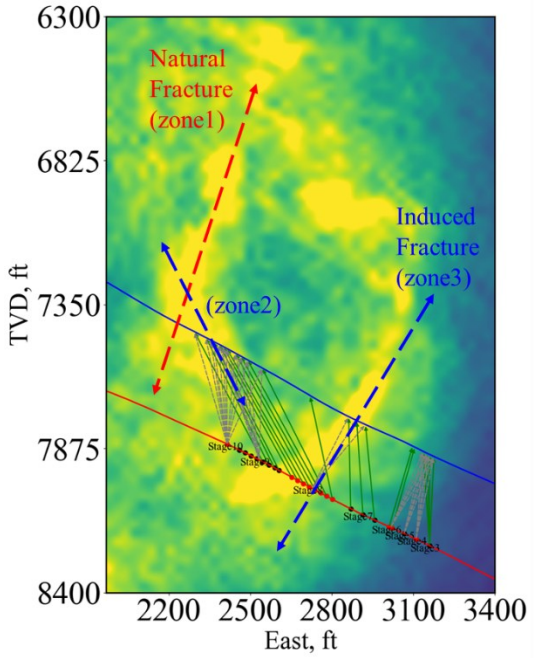

Figure 19: Fracture reflection imaging derived from MEQ sources and inferred fracture orientation. Green arrows indicate newly generated hydraulic fractures in the current stage, while gray arrows indicate reactivated (reopened) hydraulic fractures that were initially generated in previous stages.

6. DISCUSSION

To summarize, three potential fracture propagation paths are proposed in Figure 10(b) to explain why fracture hits in stage 8 occurred obliquely above the perforation locations. These paths correspond to different mechanisms, including cement debonding along the treatment well, local stress heterogeneity, and cement debonding along the monitor well. Assuming path (b) in Figure 10(b), a consistent

interpretation is obtained across fiber-optic data analysis, forward geomechanics simulations, and microseismicity observations. As a supplement to the dip-angle analysis for Stages 8–10, Bunger et al. (2022) also showed that hydraulic fractures can dip at least 20° from the horizontal plane based on in-situ stress analysis, although their core samples were obtained near the toe.

In contrast, under path (a), two implications would follow: (1) The fracturing fluid is expected to migrate along the cement debonding in the treatment well, enter a natural fracture, propagate along the fracture, and eventually reach the monitoring well, where it intersects the wellbore nearly perpendicularly; and (2) microseismicity would be expected to initiate near the treatment well and progressively migrate toward the monitoring well along the natural fracture. However, the first implication is not supported by the strain response pattern in Figure 13, which shows that fractures intersect the monitoring well at an angle of approximately 34°, corresponding to a fracture dip angle of about 60°. The second implication is inconsistent with the observations in Figure 17(b). Moreover, path (a) cannot explain the microseismic trend highlighted by the green ellipse in Figure 16.

Path (c) can be excluded based on the fiber-optic data analysis. As shown in Figure 13 for Stage 8, the strain-rate waterfall exhibits a distinct asymmetric heart-shaped pattern, indicating that the induced fracture propagated from a remote location and intersected the fiber, rather than being initiated at the fracture-hit location. Had the fracture originated at the monitor well (i.e., at the fiber location), it would not produce a heart-shaped pattern in the fiber-measured strain-rate waterfall.

Overall, path (b) provides the most consistent and plausible interpretation of fracture propagation at the site.

7. CONCLUSION

The Utah FORGE site represents a valuable EGS project characterized by complex deformation geometry and a comprehensive set of field measurements. In this study, we mapped the hydraulic fracture propagation pathway across all stages and the intersection between hydraulic fracture and natural fracture combining fiber-optic data analysis, forward geomechanical simulations, and microseismicity observations. Based on this integrated analysis, the following key conclusions are drawn for the Utah FORGE site:

Cross-well fiber-optic data analysis:

1. A total of 21 hydraulic fractures are identified from the fiber-optic data.
2. The spatial distribution of identified fractures is clustered into three groups, with average fracture-hit spacings of 31 ft, 34 ft, and 15 ft, respectively.
3. Pre-existing fractures are reactivated in most stages, and the induced fracture-to-cluster ratio varies from 0 to 4.
4. The average time for newly generated fractures to reach the fiber is 132 min, while the average time for pre-existing fracture reopening is 64 min.
5. Assuming the fracture strike aligns with S_{Hmax}, hydraulic fractures are nearly vertical/subvertical in Stages 3–7, while fracture dip angles are close to 60° in Stages 8–10.

Forward geomechanics simulation:

1. The forward geomechanics model is set up based on the well trajectory in field data and in-situ stress analysis.
2. A fracture dip angle of 60° from horizontal reproduces the asymmetric heart-shaped strain-rate pattern in Stage 8, consistent with field observations.

Microseismicity observations:

1. Hydraulic fractures in Stages 3–7 are largely consistent with the distribution of microseismic events, exhibiting vertical or subvertical orientations.
2. In stage 8-9, the hydraulic fractures propagated directly toward the identified fracture hit locations with a dip angle of about 60°.
3. In Stage 8, the propagating hydraulic fracture intersected the pre-existing natural fracture/fault plane, reactivating it and generating a large number of microseismic events.

Beyond site-specific findings, this study demonstrates broader applicability for future EGS projects. It provides a workflow for fracture-geometry characterization by integrating multiple diagnostic methods and highlights the value of distributed fiber-optics strain sensing for monitoring strain responses with high spatial and temporal resolution.

Acknowledgement

The lead authors gratefully acknowledge financial support from the Advanced Geomechanics Fracture & Reservoir Application Consortium (AGFRAC) at Texas A&M University. The authors also thank the Neubrex Energy Services and Geothermal Data Repository

(GDR) for providing access to the data used in this study. Co-authors Y. Ma and J. Ajo-Franklin were supported by DOE EERE, Geothermal Technologies Office, through funding to Utah FORGE and the University of Utah under Project DE-EE0007080 "Enhanced Geothermal System Concept Testing and Development at the Milford City, Utah Frontier Observatory for Research in Geothermal Energy (Utah FORGE) site". We appreciate the assistance and support of the FOGMORE@Utah FORGE team, Utah FORGE project 3-2417.

REFERENCES

Ajo-Franklin, J., Becker, M., Chamarczuk, M., et al.: Distributed fiber-optic sensing deployment in a deep EGS production well at Utah FORGE: Preliminary results and lessons learned. In 50th Workshop on Geothermal Reservoir Engineering, Stanford, CA, (2025).

Bao, X., and Eaton, D.W.: Fault activation by hydraulic fracturing in western Canada, Science, 354, (2016), 1406–1409.

Bunger, A., Higgins, J., Huang, Y., Kelley, M.: Core-Based In-Situ Stress Estimation for Utah FORGE Well 16A(78)-32 using Triaxial Ultrasonic Velocity and Deformation Rate Analysis, Technical Report, Utah FORGE, 120 pp., 2024. Available at: https://gdr.openei.org/submissions/1438

Haffener, J., et al.: Did we break new rock? Utilizing diagnostics to differentiate new fracture creation vs old fracture reactivation: A Meramec and Wolfcamp study. In SPE Hydraulic Fracturing Technology Conference and Exhibition, p. D021S006R002. SPE, 2022.

Jin, G., and Roy, B.: Hydraulic-fracture geometry characterization using low-frequency DAS signal. The Leading Edge, 36(12), (2017), 975–980.

Jurick, D., Alan R., and Mukul M.S.: Improving the connectivity between injection and production wells in enhanced geothermal systems using fiber optic data. In SPE Hydraulic Fracturing Technology Conference and Exhibition, p. D031S008R003. SPE, 2025.

Karrenbach, M., Cole, S., Ridge, A., et al.: Fiber-optic distributed acoustic sensing of microseismicity, strain and temperature during hydraulic fracturing. Geophysics, 84(1), (2019), D11–D23.

Liu, Y.: Hydraulic fracture geometry characterization using low-frequency distributed acoustic sensing data: Forward modeling, inverse modeling, and field applications. PhD diss., Texas A&M University, 2021.

Ma, Y., et al.: Geothermal reservoir characterization at Utah FORGE using DAS microseismic imaging. Journal of Geophysical Research: Solid Earth, 131(1), (2026), e2025JB032603.

Maxwell, S.C.: Microseismic Imaging of Hydraulic Fracturing, SEG Distinguished Instructor Series No. 17, (2014).

McClure, M.W.: Preliminary Analysis of Results from the Utah FORGE Project. In Proceedings of the 50th Workshop on Geothermal Reservoir Engineering, Stanford University, (2025), pp. 10–12.

Ning, Y., and Jin, G.: Enhancing unconventional reservoir development through low-frequency distributed acoustic sensing technology. Distributed Acoustic Sensing in Borehole Geophysics, (2024), 499–530.

Ou, Y., et al.: Evaluating fluid circulation in enhanced geothermal systems at the FORGE site using thermo-hydro-mechanical models and fiber-optic distributed strain measurements. SPE Annual Technical Conference and Exhibition. SPE, 2024.

Podgorney, R.: Reference Native State and Stimulation Models of the Utah FORGE Site. In Stanford Geothermal Workshop, 2020.

Rutqvist, J., Rinaldi, A.P., Cappa, et al.: Modeling of fault reactivation and induced seismicity during hydraulic fracturing of shale-gas reservoirs. Journal of Petroleum Science and Engineering, 107, (2013), 31–44.

Scholz, C.H.: The Mechanics of Earthquakes and Faulting (3rd ed.), Cambridge University Press, (2019).

Song, X., Ge, J., et al.: Field Data Interpretation of Cross-Well Strain Measurements with Slippage Effect Using Single-Use Fiber in the Anadarko Basin. In SPE Hydraulic Fracturing Technology Conference and Exhibition, p. D021S006R006. SPE, 2025.

Warpinski, N.R.: Microseismic monitoring: Inside and out, Journal of Petroleum Technology, 61, (2009), 80–85.

Wu, K., Liu, Y., Jin, G., et al.: Fracture hits and hydraulic-fracture geometry characterization using low-frequency distributed acoustic sensing strain data. Journal of Petroleum Technology, 73(07), (2021), 39–42.

Xing, P., Wray, A., Velez-Arteaga, et al.: In-situ stresses and fractures inferred from image logs at Utah FORGE. In Proceedings of the 47th Workshop on Geothermal Reservoir Engineering, Stanford University, Stanford, California, USA, (2022), pp. 7–9.

Xing, P., et al.: Analysis of the 2024 Circulation Tests at Utah FORGE and the Response of Fiber Optic Sensing Data. 50th Workshop on Geothermal Reservoir Engineering, Stanford University, Stanford, California, 2025.

Zhang, W., Wang, Z., Guo, T., et al.: The enhanced geothermal system heat mining prediction based on fracture propagation simulation of thermo-hydro-mechanical-damage coupling: Insight from the integrated research of heat mining and supercritical CO_2 fracturing. Applied Thermal Engineering, 215, (2022), 118919.

Zoback, M.D.: Reservoir Geomechanics, Cambridge University Press, (2010).